nature physics

LETTERS

https://doi.org/10.1038/s41567-021-01217-z

Check for updates

One-dimensional Kronig–Penney superlattices at the $LaAlO_3/SrTiO_3$ interface

Megan Briggeman[1,2], Hyungwoo Lee[3], Jung-Woo Lee[3], Kitae Eom[3], François Damanet[2,4,5], Elliott Mansfield[2,4], Jianan Li[1,2], Mengchen Huang[1,2], Andrew J. Daley[2,4], Chang-Beom Eom[3], Patrick Irvin[1,2] and Jeremy Levy[1,2]✉

Semiconductor heterostructures[1] and ultracold neutral atomic lattices[2] capture many of the essential properties of one-dimensional electronic systems. However, fully one-dimensional superlattices are highly challenging to fabricate in the solid state due to the inherently small length scales involved. Conductive atomic force microscope lithography applied to an oxide interface can create ballistic few-mode electron waveguides with highly quantized conductance and strongly attractive electron–electron interactions[3]. Here we show that artificial Kronig–Penney-like superlattice potentials can be imposed on such waveguides, introducing a new superlattice spacing that can be made comparable to the mean separation between electrons. The imposed superlattice potential fractures the electronic subbands into a manifold of new subbands with magnetically tunable fractional conductance. The lowest plateau, associated with ballistic transport of spin-singlet electron pairs[3], shows enhanced electron pairing, in some cases up to the highest magnetic fields explored. A one-dimensional model of the system suggests that an engineered spin–orbit interaction in the superlattice contributes to the enhanced pairing observed in the devices. These findings are an advance in the ability to design new families of quantum materials with emergent properties and the development of solid-state one-dimensional quantum simulation platforms.

Quantum theory provides a unified framework for understanding the fundamental properties of matter. However, there are many quantum systems whose behaviour is not well understood because the relevant equations cannot be solved using known approaches. The idea of 'quantum simulation', first articulated by Feynman[4], aims to exploit the quantum-mechanical properties of materials to compute the properties of interest and gain an insight into the quantum nature of matter. There are two main 'flavours' of quantum simulation: one based on the known efficiency of circuit-based quantum computers to solve the Schrödinger equation, and the other based on microscopic control over quantum systems to emulate a given Hamiltonian. The former approach is limited by the capabilities of present-day quantum computers. The latter approach has shown great promise using a variety of methods including ultracold atoms[2,5,6], spin systems from ion-trap arrays[7], superconducting Josephson junction arrays[8], photonic systems[9] and various solid-state approaches[1,10–12]. Platforms capable of quantum simulation of Hubbard models would be of enormous value in condensed matter physics and beyond.

Complex oxides offer new opportunities to create a platform for quantum simulation in a solid-state environment. Their complexity gives access to quantum phases of matter, such as superconductivity, where the model Hamiltonians (for example, two-dimensional Hubbard model) are challenging to understand theoretically. In addition, their nanoscale reconfigurability makes it possible to engineer new forms of quantum matter with extreme nanoscale precision[13,14].

Here we present experiments that contribute to a solid-state quantum simulation platform based on a reconfigurable complex-oxide material system. Using conductive atomic force microscope (c-AFM) lithography, we create Kronig–Penney-like[15] one-dimensional (1D) superlattice structures by spatially modulating the potential of a 1D electron waveguide device at the interface. Further, c-AFM lithography has been used to create a variety of devices at the $LaAlO_3/SrTiO_3$ interface[16]. A c-AFM tip—moving in contact with the $LaAlO_3$ surface and positively biased with respect to the interface—locally creates ('writes') conducting regions at the interface (Fig. 1a), while a negatively biased tip locally restores ('erases') the interface to an insulating state. This technique achieves nanoscale control, with precision as high as 2 nm (ref. [14]), over the conductivity of the interface and most of its properties.

The work described here concerns electron waveguide devices[3] that have been perturbed by a spatially periodic potential, similar to the one first envisioned by Kronig and Penney[15]. Unperturbed waveguides exhibit highly quantized ballistic transport with conductance steps at or near integer values of the conductance quantum e^2h^{-1}, where e is the electron charge and h is the Planck constant. The subband structure of electron waveguides can be described by a waveguide model that takes into account the vertical, lateral and spin degrees of freedom[3]. Representative orbitals for electron waveguides, subject to parabolic lateral confinement and half-parabolic vertical confinement, are shown in Fig. 1b, where $|m, n, s\rangle$ is a state specified by quantum numbers m, n and s that correspond to the number of lateral (m) and vertical (n) modes of the wavefunction and spin s. The complete set of states form a basis for describing extended states along the waveguide direction x. The periodic modulation of the waveguide may couple different vertical modes (for example, those highlighted in black in Fig. 1b) with the ground state $|0, 0, \uparrow\rangle$. Due to attractive electron–electron interactions, subband energy minima can 'lock' together to form electron pairs[3] that also propagate ballistically. Pairing in electron waveguides arises from the same electron–electron interactions that give rise to superconductivity[17]. In some cases, more exotic locking of subbands can

[1]Department of Physics and Astronomy, University of Pittsburgh, Pittsburgh, PA, USA. [2]Pittsburgh Quantum Institute, Pittsburgh, PA, USA. [3]Department of Materials Science and Engineering, University of Wisconsin-Madison, Madison, WI, USA. [4]Department of Physics and SUPA, University of Strathclyde, Glasgow, UK. [5]Institut de Physique Nucléaire, Atomique et de Spectroscopie, CESAM, University of Liège, Liège, Belgium. ✉e-mail: jlevy@pitt.edu

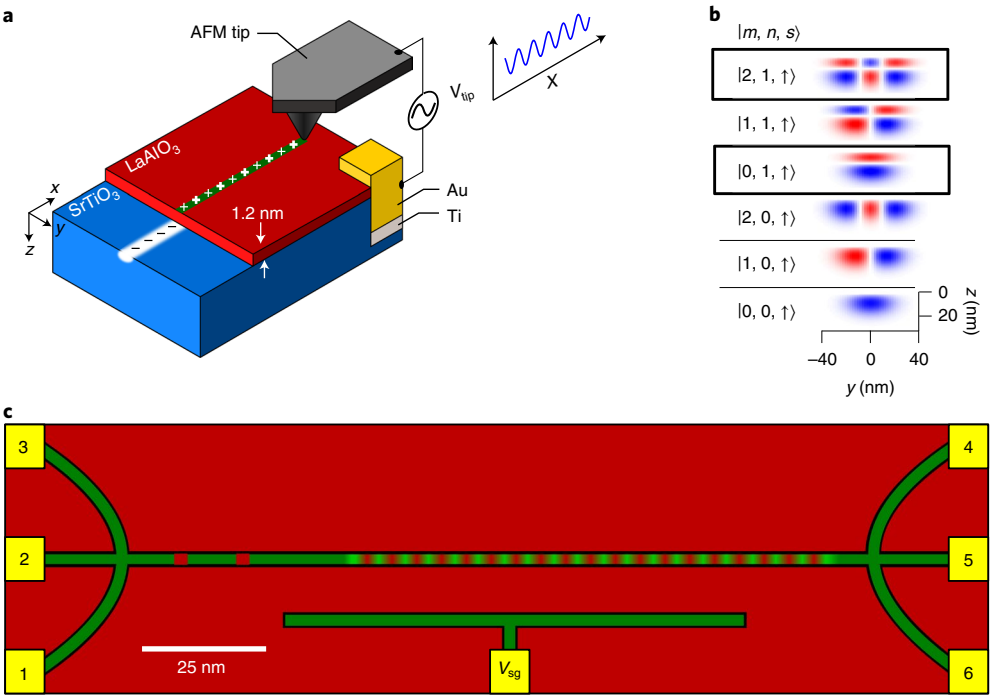

Fig. 1 | Schematic of c-AFM writing and 1D superlattice device. a, Writing schematic of the c-AFM. A positive bias on the AFM tip protonates the $LaAlO_3$ surface, locally creating a conducting channel at the interface. **b**, Table showing different representative wavefunctions calculated using a single-particle model for electron waveguide devices[3]. The imposed vertical superlattice structure may cause mixing of the vertical modes of an electron waveguide device, mixing the ground state with the modes highlighted in black. **c**, Schematic of a 1D vertical superlattice device. The superlattice is created by first writing the main channel with a positive tip voltage. The same path is then traced while applying a sinusoidal tip voltage to periodically modulate the confining potential of the device. The superlattice is created in series with two highly transparent tunnel barriers.

occur, for example, the Pascal conductance plateaus that indicate the binding of $n \geq 2$ electron states[18]. The presence of strong, tunable electron–electron interactions[19] makes these electron waveguide devices an interesting starting point for engineering 1D quantum systems.

One-dimensional superlattice devices are created by first writing a conductive nanowire with a constant positive voltage applied to the atomic force microscope (AFM) tip ($V_{tip} \approx 10$ V). This path is re-traced along the same direction while applying a sinusoidally varying tip voltage $V_{tip}(x) = V_0 + V_k \sin(kx)$, where V_0 is a d.c. voltage, V_k is the amplitude of the sinusoidal voltage and k is the spatial frequency of the sinusoidal signal producing a spatially periodic potential modulation. A short unpatterned waveguide is written in series next to the superlattice, which helps in controlling the chemical potential in the device structure[3]. Four-terminal magneto-transport measurements are carried out in a dilution refrigerator at or near its base temperature in the range of $T \approx 15$–50 mK, unless otherwise indicated. Data are presented for three 1D superlattice devices, namely, devices A, B1 and B2, and two control devices (straight electron waveguides without superlattice modulation), namely, devices C1 and C2.

Figure 2a shows the transconductance dG/dV_{sg} as a function of out-of-plane magnetic field B and side-gate voltage V_{sg} for device A. The transconductance map provides a visual indication of the subband structure. Purple regions, where the transconductance is nearly zero, represent conductance plateaus. Bright coloured (red/yellow/green/blue) regions signify increases in conductance that generally correspond to the emergence of new subbands. White regions indicate negative transconductance, which is associated with non-monotonic behaviour in the range of $4\,T < |B| < 7\,T$. The transconductance is generally found to be highly symmetric with respect to the applied magnetic field. Figure 2b shows a series of conductance curves versus V_{sg} for a sequence of out-of-plane magnetic fields B, ranging between 0 T (leftmost) to 16 T (rightmost). Curves are offset by $\Delta V_{sg} \approx 7.5\,mV\,T^{-1}$ for clarity and curves at 1 T intervals are highlighted in black. At low magnetic fields ($|B| \approx 2$ T), a plateau at around 1.80 e^2h^{-1} develops before bifurcating into two distinct plateaus, one of which decreases in value, while the other increases towards a nearly quantized value of $1.99e^2h^{-1}$. The onset of the two plateaus can be clearly seen in the transconductance (Fig. 2a) as a minigap that appears in the lowest subband.

In addition to the plateau at 2 e^2h^{-1}, many other subband features are readily seen at higher conductance values. Close ups of three selected areas (Fig. 2c–e) reveal several conductance plateaus. Conductance increases between these plateaus correspond to new subbands—the so-called 'fractured' states—that become available in the transconductance map. These appear to be fractional subbands as the increase in conductance between the plateaus are fractions of the conductance quanta e^2h^{-1}. Figure 2e shows the fractional conductance feature occurring below the 2 e^2h^{-1} plateau in more detail. The feature first appears in the form of a conductance peak and then bifurcates forming the 2 e^2h^{-1} plateau, and a lower fractional conductance feature that evolves with the magnetic field.

Data for the second superlattice device (device B1; Extended Data Fig. 1) yield qualitatively similar behaviour. The overall subband structure resembles the subband structure of an electron waveguide device with no superlattice patterning, but the subbands are, similar to device A, fractured into additional manifolds with fractional conductance plateaus, including a plateau at 2 e^2h^{-1} (Extended Data Fig. 2). Device B1 also shares the prominent highly quantized conductance plateau at 2 e^2h^{-1}. We present the third device (device B2; Extended Data Fig. 3) that also exhibits fractional conductance plateaus (Supplementary Information).

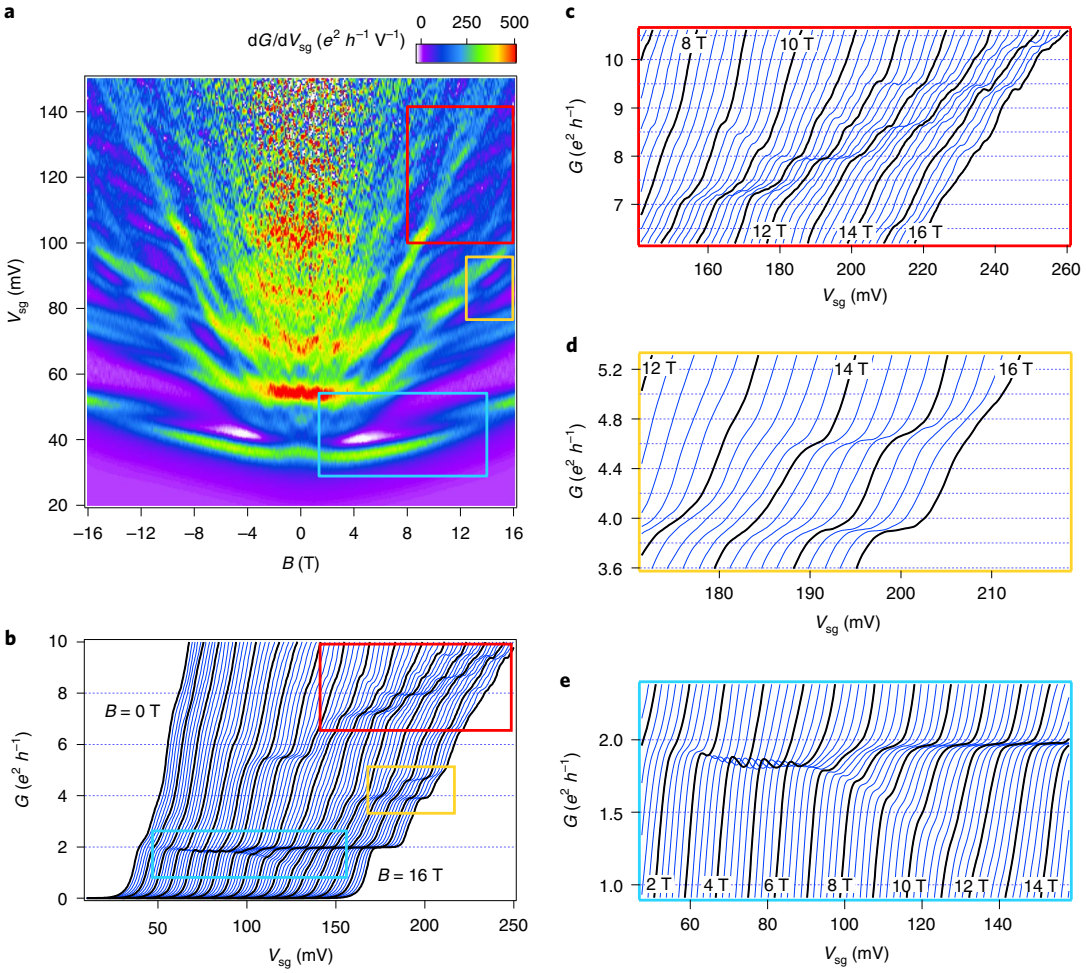

Fig. 2 | Magnetotransport characteristics and fractional conductance features. a, Transconductance dG/dV_{sg} is plotted as a function of magnetic field B and side-gate voltage V_{sg}. Purple regions indicate zero transconductance (conductance plateaus). Bright regions indicate increasing conductance—energies where new 1D subbands become available. Negative transconductance is indicated in white, mainly in two lobes above the $2\ e^2h^{-1}$ plateau near 5 T. Regions highlighted in coloured boxes are a guide to the eye, indicating the location of the conductance curves. **b**, Conductance G versus side-gate voltage V_{sg} at magnetic fields ranging from $B = 0$ T to 16 T. Curves are offset by $\Delta V_{sg} \approx 7.5$ mV T^{-1} for clarity. Curves at 1 T intervals are highlighted in black. Coloured boxes indicate the corresponding locations in **a** and **c**–**e**. **c**,**d**, Conductance curves showing the conductance plateaus that correspond to the 'fractured' states in the transconductance map. The conductance jump between the plateaus are fractions of the conductance quanta e^2h^{-1}. **e**, Conductance curves highlighting the fractional conductance feature occurring below the $2\ e^2h^{-1}$ plateau. Data shown are for device A and taken at $T = 15$ mK.

Finite-bias spectroscopy data of device A (Extended Data Fig. 4) reveal a characteristic diamond structure in the transconductance. This feature is associated with clean ballistic transport[20,21] and is due to unevenly populated subbands at large finite biases that give rise to half plateaus. The diamond visible in the transconductance corresponds to a fractional conductance feature below the $2\ e^2h^{-1}$ plateau at around $0.5\ e^2h^{-1}$ at zero bias and about half that value at finite bias. The presence of this characteristic diamond structure makes it unlikely that the fractional features are due to trivial causes, for example, reduced transmission due to partial reflection at one end of the nanowire. Finite-bias spectroscopy data of device B2 also feature a similar diamond structure, as shown in Extended Data Fig. 5.

Unmodulated control devices (two of which are shown in Extended Data Fig. 6 and more than ten are published elsewhere[3,18]) do not exhibit fractional conductances. The characteristic behaviour of such control electron waveguide devices is a series of conductance plateaus that are quantized in integer values of e^2h^{-1}, that is, lacking the fractionalized subbands observed here.

Fractional conductances in 1D transport have been reported in a variety of systems, and this phenomenon generally arises when there are strong electron–electron interactions. The fractional quantum Hall state[22] is perhaps the best known and most investigated example. The 0.7 anomaly[23] in quantum point contacts[24,25] has been extensively investigated. Electron–electron interactions are believed to play a central role in the formation of the conductance plateau observed at $0.7 \times (2\ e^2h^{-1})$ (ref. [26]). Fractional conductances have been observed in several 1D quantum wire systems such as strained Ge-based hole quantum wires[27] and GaAs-based quantum wires[28].

Shavit et al. have considered a theoretical framework[29,30] in which fractional conductances arise in multichannel 1D quantum wires due to high-order backscattering processes. Such fractional conductances were shown to require strong repulsive electron–electron interactions to be observed, but a recent theory suggests that this could also be the case for strong attractive modulated interactions[31]. For the simplest high-order scattering process involving three particles, this theory predicts a plateau at $1.8\ e^2h^{-1}$, which can become gap protected for strong modulated interactions. Our observation of a stable conductance plateau near $1.8\ e^2h^{-1}$ near $B = 2$ T, together with its absence in unmodulated waveguides, is consistent with this prediction.

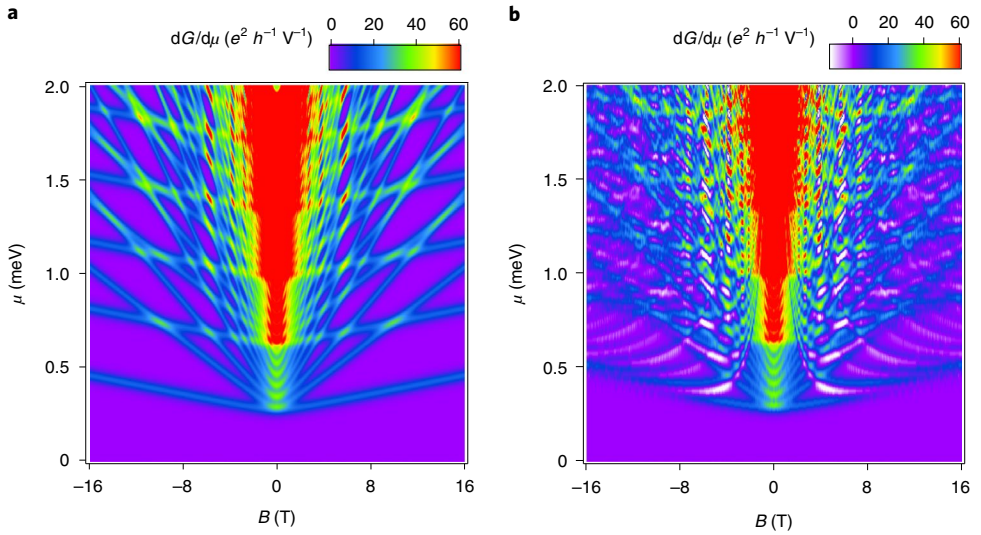

Fig. 3 | Waveguide models. a, Transconductance spectra for a non-interacting single-particle electron waveguide model. **b**, Transconductance spectra for an electron waveguide with vertical modulation characterized by period $\lambda_M = 10$ nm and potential strength $V = 0.075$ meV. Effective broadening energy is 0.015 meV. Other parameters for both **a** and **b**: $m_x = m_y = 1.9 m_e$, $m_z = 6.5 m_e$, $g = 0.62$, $l_z = 8.1$ nm and $l_y = 26.0$ nm, where m_x, m_y and m_z are the effective masses along the x, y and z directions, m_e is the electron mass, g is the Landé factor, l_y is the waveguide width and l_z is the waveguide depth into $SrTiO_3$.

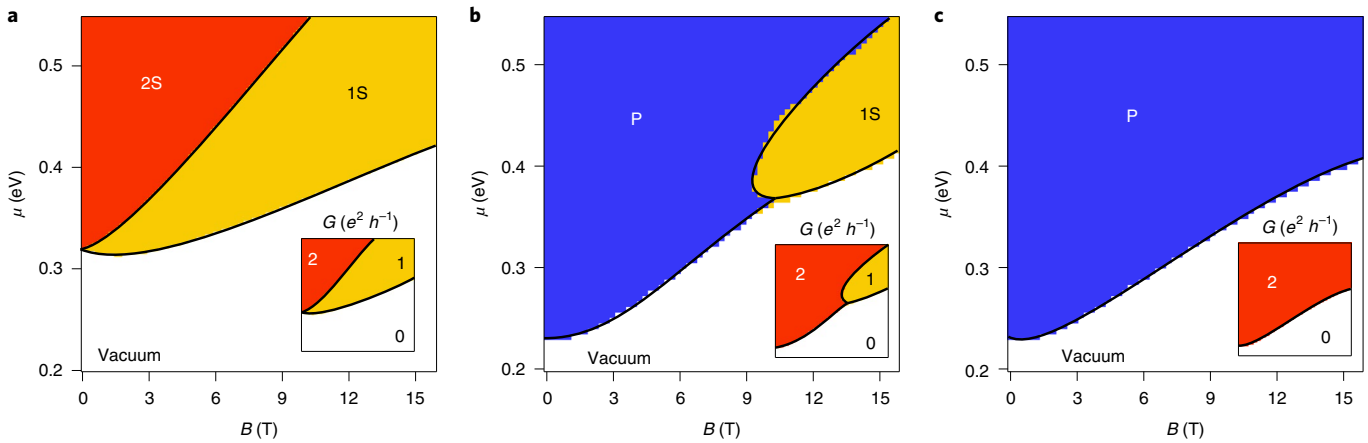

Fig. 4 | Phase diagrams of the mean-field model. a–c, Phase diagrams of the waveguide obtained from equation (1) as a function of magnetic field B and chemical potential μ for different electron–electron interactions U and spin–orbit couplings α_{so}. **a**, No interaction ($U(0) = 0$ meV nm) and no spin–orbit coupling ($\alpha_{SO} = 0$ meV nm). The areas labelled as 'vacuum', '1S' and '2S' correspond to an empty phase, a single-particle phase and two single-particle phases, respectively. The phases are delimited by the Zeeman-split single-particle energies $\xi_{\sigma k}(B, \mu)$ of the states $|0, 0, \downarrow\rangle \otimes |k\rangle$ and $|0, 0, \uparrow\rangle \otimes |k\rangle$ (Supplementary Information provides detailed expressions) satisfying $\xi_{\sigma 0}(B, \mu) = 0$ (solid black lines). The inset shows the associated conductance. **b**, Finite interaction ($|U(0)| = 4.2$ meV nm) and small spin–orbit coupling ($\alpha_{SO} = 0.05$ meV nm), accounting for a potential intrinsic Rashba spin–orbit coupling. The presence of interactions induces pairing Δ of the orbitals in some region of parameters (phase 'P'), moving the splitting of the two single-particle bands to a higher magnetic field ($B \approx 10$ T). This diagram corresponds to typical unmodulated waveguides with large pairing fields (Extended Data Fig. 6). **c**, Finite interaction ($|U(0)| = 4.2$ meV nm) and larger spin–orbit coupling ($\alpha_{SO} = 0.25$ meV nm). The enhanced spin–orbit coupling increases the area of the paired phase up to $B \approx 16$ T. This spin–orbit-assisted pairing phenomenon is not sensitive to the specific parameter values.

A defining characteristic of the system is the prevalence of strong attractive electron–electron interactions[3,17–19]. Both vertical superlattice devices show signs of (weak) superconductivity at $B = 0$ T (Extended Data Fig. 7). Empirically, unperturbed electron waveguides (which possess attractive interactions) do not exhibit fractional conductance plateaus. Devices at the interface exhibit electron pairing without superconductivity[3,17]. In electron waveguides, this interaction causes electron subband energy minima to lock together, either near the zero magnetic field or at re-entrant values, resulting in conductance steps of $2\,e^2\,h^{-1}$.

The superlattice modulation of electron waveguides is empirically linked to enhanced electron pairing fields: superlattice devices have been observed with pairing fields of $B_p > 16$ T, substantially higher than control devices written in the same area of the sample. The largest pairing field observed in an unmodulated waveguide is $B_p \approx 11$ T (ref. [3]). The enhanced pairing strength appears to be influenced by the potential modulation, but a direct correlation is obscured by other variations between devices. Superlattices formed by lateral modulation do not show an enhanced pairing field[32].

Another effect that is correlated with vertical modulation is a spin–orbit-like effect in the device. The lowest subband in device A (seen in the transconductance map in Fig. 2a) bends upwards at zero magnetic field; therefore, the minima of the lowest subband are at a finite magnetic field. This may be due to the engineering of a spin–orbit field, and it is not usually observed in quasi-1D electron waveguide devices at the interface. As the electrons travel through the device with momentum $\mathbf{k} = k\hat{x}$, the periodic vertical modulation will create an effective electric field $\mathbf{E}_{\mathrm{eff}}(x) = E_0 \sin(kx)\hat{z}$, which will yield an effective spin–orbit field $\mathbf{B}_{\mathrm{SO}} \propto \mathbf{k} \times \mathbf{E}_{\mathrm{eff}}$ in the $\hat{y}$ direction. This could result in a coupling between the spin-up and spin-down particles, which may also be the mechanism for enhancing the pairing field in these devices. Note that the interface is known to exhibit an intrinsic Rashba spin–orbit coupling[33,34], but theoretical models suggest that confinement along a nanowire could significantly reduce it[35]. The measurements presented here suggest that a non-negligible value of spin–orbit coupling could be restored when the modulation is present.

We present below a minimal model that provides a basic description of two of the features generated by a modulated waveguide: the fracture of the first conductance line and enhanced spin–orbit coupling. Figure 3a shows a calculated transconductance map for a single-particle model of a straight, unmodulated electron waveguide, described in more detail elsewhere[3]. In this model, the states $|m, n, s\rangle \otimes |k\rangle$ are characterized by single-particle energies $\xi_{mn\sigma k}$ (see equation (1) in Supplementary Information), where $\sigma = \downarrow$ ($\uparrow$) for $s = -1/2$ (1/2). Transconductance lines appear for $\xi_{mn\sigma 0} = 0$, that is, when the chemical potential reaches the bottom of the bands. The waveguide model shows an overall resemblance to the experimental data for the superlattice (Fig. 2a), except that the subbands are fractured into a manifold of new states with fractional conductances. These fractures can be qualitatively accounted for by adding a Kronig–Penney potential to the model (Supplementary Information). In this model, the potential creates bandgaps in each subband single-particle spectrum, which appear when the Fermi wavelength of an electron in a given subband corresponds to a fraction of the modulation period. Figure 3b shows the corresponding transconductance map, where the bandgaps translate into curved lines above each subband, which notably exhibit negative regions. This interference effect is particularly reminiscent of the fracture observed in the first transconductance line in Fig. 2a, which suggests that it is the basis of the behaviour observed in the experiments. This single-particle Kronig–Penney model cannot predict the full fractional conductance plateaus, which are understood to require the presence of strong electron–electron interactions[29–31].

As noted above, the modulation can also produce an enhanced spin–orbit interaction, and we can investigate the potential consequences of this in a 1D model for the two first orbitals, namely, $|0, 0, \downarrow\rangle$ and $|0, 0, \uparrow\rangle$, with a spin–orbit coupling term of the form $H_{\mathrm{so}} = \alpha_{\mathrm{so}} k \sigma_y$, and to simplify the calculations, with no spatial dependence of the spin–orbit coupling strength α_{so}. Here we neglect the bandgaps produced by the modulation to focus on the effect of the spin–orbit coupling alone. Starting from a model with Hubbard interactions, in the mean-field approximation, our Hamiltonian in momentum space[3] reads

$$H = \sum_k \Big[\sum_\sigma (\xi_{00\sigma k} + \Sigma_\sigma) c^\dagger_{\sigma k} c_{\sigma k} + \Delta (c^\dagger_{\uparrow k} c^\dagger_{\downarrow -k} - c_{\uparrow k} c_{\downarrow -k}) + (i\alpha_{\mathrm{so}} k - \chi_{\downarrow\uparrow}) c^\dagger_{\uparrow k} c_{\downarrow k} - (i\alpha_{\mathrm{so}} k + \chi_{\uparrow\downarrow}) c^\dagger_{\downarrow k} c_{\uparrow k} \Big], \quad (1)$$

where $c_{\sigma k}$ is the annihilation operator of an electron with momentum k and spin σ in the transverse mode $|0, 0\rangle$ ($\sigma = \downarrow, \uparrow$), and Σ_σ, Δ and $\chi_{\sigma\bar{\sigma}}$ are the Hartree shifts, pairing order parameter, and Fock fields, respectively, which are defined as

$$\Sigma_\sigma = \tfrac{U}{2\pi} \int \langle c^\dagger_{\bar{\sigma} k} c_{\bar{\sigma} k} \rangle \mathrm{d}k, \qquad \Delta = \tfrac{U}{2\pi} \int \langle c_{\downarrow -k} c_{\uparrow k} \rangle \mathrm{d}k, \qquad \chi_{\sigma\bar{\sigma}} = \tfrac{U}{2\pi} \int \langle c^\dagger_{\sigma k} c_{\bar{\sigma} k} \rangle \mathrm{d}k, \quad (2)$$

where $U \equiv U(B) < 0$ is an attractive electron–electron interaction (in units of energy × length) rescaled by the magnetic field and $\bar{\sigma}$ denotes the opposite spin of σ (Supplementary Information). The mean fields are found self-consistently, and they indicate the presence of electrons and paired electrons (though not superconductivity in this 1D model) in the waveguide. Calculating these values determines phase diagrams for different values of α_{so} and U. Our results are shown in Fig. 4. We find an enhanced pairing area, defined as the region of non-zero Δ, for increasing α_{so}. This minimal model (which could be extended to position-dependent potentials and spin–orbit coupling) thus supports the idea that a spin–orbit coupling engineered by the experimental setup can increase the pairing of the two lowest subbands $|0, 0, \downarrow\rangle$ and $|0, 0, \uparrow\rangle$ up to a higher magnetic field, yielding a first conductance step of $2\,e^2 h^{-1}$. A similar effect (that is, an enhanced spin–orbit coupling) is seen in lateral 1D superlattice devices[32]. However, the engineered spin–orbit coupling in the lateral superlattice devices does not lead to enhanced pairing. This can be understood since in our framework, a lateral modulation creates a spin–orbit field B_{SO} along the quantization axis z and hence does not directly couple the spin-up and spin-down electrons, which is in contrast to the case of vertical modulation.

Kronig–Penney devices described here also show variations in properties, but the fractional plateaus are not observed in any of the unmodulated quantum devices. Moreover, $SrTiO_3$ has well-known ferroelastic distortions below $T = 105$ K, which can impact the electronic structure of unmodulated quantum wires; the distortions are believed to play a role in parameter variations between unmodulated nanowires created under nominally identical conditions[18]. Experiments performed on nanoscale crosses[36] show highly reproducible behaviour, which is attributed to the pinning of ferroelastic domains in the insulating regions by the nanocross structure.

The theoretical analysis presented above suggests that spin–orbit interactions increase the effective pairing strength in the Kronig–Penney nanowires. Because of natural variations in the device parameters, it is not possible to conclude that this effect is experimentally observed. Future experiments that can constrain the ferroelastic domains surrounding the device, coupled with systematic variations in modulation amplitude and spatial frequency, may provide more definitive answers to these questions.

The ability to create new superlattice structures, and modulate interactions in 1D systems, opens new frontiers in the development of quantum matter. The systems created here focus on low-dimensional confined structures, which are challenging to create using other methods. The regular superlattice structure can be replaced with quasi-periodic order, artificially imposed disorder, topological defects or combined with lateral perturbations, which are a few possibilities. Unlike the Kronig–Penney description, electron–electron interactions play a defining role in the resulting quantum phases, and future discoveries of emergent phases in this family of 1D systems are highly likely.

Online content

Any methods, additional references, Nature Research reporting summaries, source data, extended data, supplementary information, acknowledgements, peer review information; details of author contributions and competing interests; and statements of data and code availability are available at https://doi.org/10.1038/s41567-021-01217-z.

Received: 12 December 2019; Accepted: 4 March 2021;
Published online: 15 April 2021

References

1. Byrnes, T., Kim, N. Y., Kusudo, K. & Yamamoto, Y. Quantum simulation of Fermi-Hubbard models in semiconductor quantum-dot arrays. *Phys. Rev. B* **78**, 075320 (2008).
2. Jaksch, D. & Zoller, P. The cold atom hubbard toolbox. *Ann. Phys.* **315**, 52–79 (2005).
3. Annadi, A. et al. Quantized ballistic transport of electrons and electron pairs in $LaAlO_3/SrTiO_3$ nanowires. *Nano Lett.* **18**, 4473–4481 (2018).
4. Feynman, R. P. Simulating physics with computers. *Int. J. Theor. Phys.* **21**, 467 (1982).
5. Mazurenko, A. et al. A cold-atom Fermi–Hubbard antiferromagnet. *Nature* **545**, 462–466 (2017).
6. Choi, J.-Y. et al. Exploring the many-body localization transition in two dimensions. *Science* **352**, 1547–1552 (2016).
7. Porras, D. & Cirac, J. I. Effective quantum spin systems with trapped ions. *Phys. Rev. Lett.* **92**, 207901 (2004).
8. Houck, A. A., Türeci, H. E. & Koch, J. On-chip quantum simulation with superconducting circuits. *Nat. Phys.* **8**, 292–299 (2012).
9. Politi, A., Matthews, J. C. F. & O'Brien, J. L. Shor's quantum factoring algorithm on a photonic chip. *Science* **325**, 1221 (2009).
10. Singha, A. et al. Two-dimensional Mott–Hubbard electrons in an artificial honeycomb lattice. *Science* **332**, 1176–1179 (2011).
11. Slot, M. R. et al. Experimental realization and characterization of an electronic Lieb lattice. *Nat. Phys.* **13**, 672–676 (2017).
12. Drost, R., Ojanen, T., Harju, A. & Liljeroth, P. Topological states in engineered atomic lattices. *Nat. Phys.* **13**, 668–671 (2017).
13. Cen, C. et al. Nanoscale control of an interfacial metal–insulator transition at room temperature. *Nat. Mater.* **7**, 298–302 (2008).
14. Cen, C., Thiel, S., Mannhart, J. & Levy, J. Oxide nanoelectronics on demand. *Science* **323**, 1026–1030 (2009).
15. Kronig, R. D. L. & Penney, W. G. Quantum mechanics of electrons in crystal lattices. *Proc. R. Soc. A* **130**, 499–513 (1931).
16. Pai, Y.-Y., Tylan-Tyler, A., Irvin, P. & Levy, J. Physics of $SrTiO_3$-based heterostructures and nanostructures: a review. *Rep. Prog. Phys.* **81**, 036503 (2018).
17. Cheng, G. et al. Electron pairing without superconductivity. *Nature* **521**, 196–199 (2015).
18. Briggeman, M. et al. Pascal conductance series in ballistic one-dimensional $LaAlO_3/SrTiO_3$ channels. *Science* **367**, 769–772 (2020).
19. Cheng, G. et al. Tunable electron-electron interactions in $LaAlO_3/SrTiO_3$ nanostructures. *Phys. Rev. X* **6**, 041042 (2016).
20. Glazman, L. I. & Khaetskii, A. V. Nonlinear quantum conductance of a lateral microconstraint in a heterostructure. *Europhys. Lett.* **9**, 263 (1989).
21. Patel, N. K. et al. Ballistic transport in one dimension: additional quantisation produced by an electric field. *J. Phys. Condens. Matter* **2**, 7247 (1990).
22. Tsui, D. C., Stormer, H. L. & Gossard, A. C. Two-dimensional magneto-transport in the extreme quantum limit. *Phys. Rev. Lett.* **48**, 1559 (1982).
23. Thomas, K. J. et al. Possible spin polarization in a one-dimensional electron gas. *Phys. Rev. Lett.* **77**, 135 (1996).
24. van Wees, B. J. et al. Quantized conductance of point contacts in a two-dimensional electron gas. *Phys. Rev. Lett.* **60**, 848 (1988).
25. Wharam, D. A. et al. One-dimensional transport and the quantisation of the ballistic resistance. *J. Phys. C* **21**, L209 (1988).
26. Bauer, F. et al. Microscopic origin of the '0.7-anomaly' in quantum point contacts. *Nature* **501**, 73–78 (2013).
27. Gul, Y., Holmes, S. N., Myronov, M., Kumar, S. & Pepper, M. Self-organised fractional quantisation in a hole quantum wire. *J. Phys. Condens. Matter* **30**, 09LT01 (2018).
28. Kumar, S. et al. Zero-magnetic field fractional quantum states. *Phys. Rev. Lett.* **122**, 086803 (2019).
29. Oreg, Y., Sela, E. & Stern, A. Fractional helical liquids in quantum wires. *Phys. Rev. B* **89**, 115402 (2014).
30. Shavit, G. & Oreg, Y. Fractional conductance in strongly interacting 1D systems. *Phys. Rev. Lett.* **123**, 036803 (2019).
31. Shavit, G. & Oreg, Y. Modulation induced transport signatures in correlated electron waveguides. *SciPost Phys.* **9**, 51 (2020).
32. Briggeman, M. et al. Engineered spin-orbit interactions in $LaAlO_3/SrTiO_3$-based 1D serpentine electron waveguides. *Sci. Adv.* **6**, eaba6337 (2020).
33. Caviglia, A. D. et al. Tunable Rashba spin-orbit interaction at oxide interfaces. *Phys. Rev. Lett.* **104**, 126803 (2010).
34. Ben Shalom, M., Sachs, M., Rakhmilevitch, D., Palevski, A. & Dagan, Y. Tuning spin-orbit coupling and superconductivity at the $SrTiO_3/LaAlO_3$ interface: a magnetotransport study. *Phys. Rev. Lett.* **104**, 126802 (2010).
35. Kim, Y., Lutchyn, R. M. & Nayak, C. Origin and transport signatures of spin-orbit interactions in one- and two-dimensional $SrTiO_3$-based heterostructures. *Phys. Rev. B* **87**, 245121 (2013).
36. Nethwewala, A. et al. Inhomogeneous energy landscape in $LaAlO_3/SrTiO_3$ nanostructures. *Nanoscale Horiz.* **4**, 1194–1201 (2019).

Methods

Pulsed laser deposition was used to grow samples with three to four unit cells of $LaAlO_3$ on $SrTiO_3$ (described in more detail elsewhere[37]). Electrical contact was made to the interface by ion milling through the interface and backfilling with Ti/Au. Further, c-AFM writing was performed by applying a voltage bias between the AFM tip and the interface, with a 1 GΩ resistor in series. Writing was performed in 30–40% relative humidity using an Asylum MFP-3D AFM. Written samples were then transferred into a dilution refrigerator and cooled to a base temperature of ~15 mK. Four-terminal measurements were performed using standard lock-in techniques at a frequency of 11 Hz with an oscillation amplitude of 1 mV. Four-terminal I–V curves were measured by applying a d.c. source–drain bias across the device.

Data availability

Source data are available at the Harvard Dataverse[38]. Other data and code that support the findings of this study are available from the corresponding author upon reasonable request.

References

37. Cheng, G. et al. Sketched oxide single-electron transistor. *Nat. Nanotechnol.* **6**, 343–347 (2011).
38. Briggeman, M. Replication data for: one-dimensional Kronig-Penney superlattices at the LAOSTO interface. *Harvard Dataverse* https://doi.org/10.7910/DVN/8IJ4QD (2021).

Acknowledgements

J. Levy acknowledges support from a Vannevar Bush Faculty Fellowship (N00014-15-1-2847) and the National Science Foundation (PHY-1913034). Work at the University of Wisconsin was supported by funding from the DOE Office of Basic Energy Sciences under award number DE-FG02-06ER46327 (C.B.E). F.D. and A.J.D. acknowledge support from the EPSRC Programme Grant DesOEQ (EP/P009565/1) and the AFOSR (FA9550-18-1-0064). F.D. acknowledges the Belgian F.R.S.-FNRS for financial support.

Author contributions

M.B., P.I. and J. Levy conducted the experiments. F.D., E.M. and A.J.D. made the theoretical model calculations. J. Li and M.H. processed the samples. H.L., J.-W.L., K.E. and C.-B.E. synthesized the thin films and performed structural and electrical characterizations. All the authors reviewed the manuscript.

Competing interests

The authors declare no competing interests.

Additional information

Extended data is available for this paper at https://doi.org/10.1038/s41567-021-01217-z.

Supplementary information The online version contains supplementary material available at https://doi.org/10.1038/s41567-021-01217-z.

Correspondence and requests for materials should be addressed to J. Levy.

Peer review information *Nature Physics* thanks Jung-Woo Yoo and the other, anonymous, reviewer(s) for their contribution to the peer review of this work.

Reprints and permissions information is available at www.nature.com/reprints.

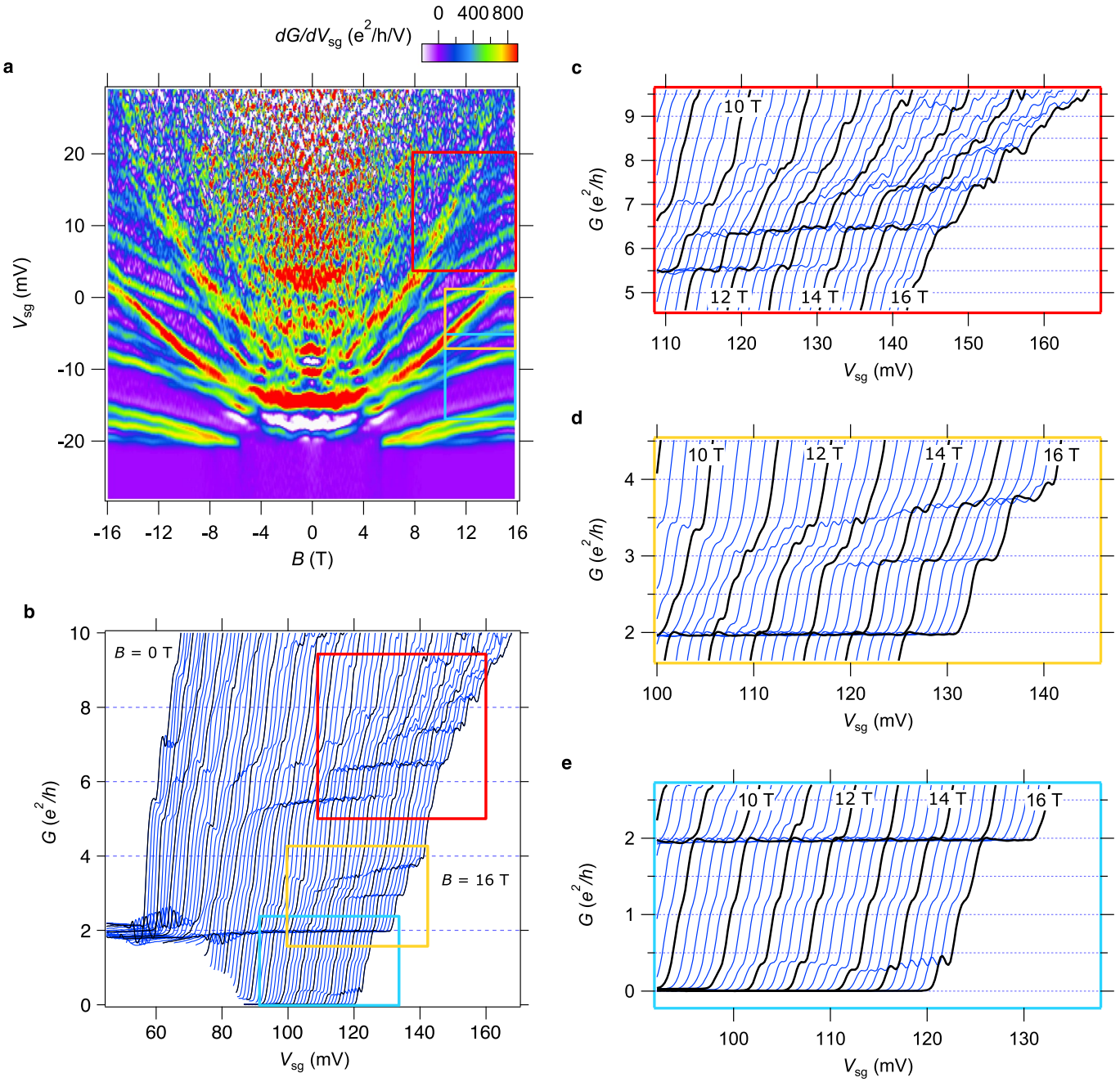

Extended Data Fig. 1 | Magnetotransport data for vertical superlattice Device B1. a, Transconductance map dG/dV_{sg} as a function of side gate voltage V_{sg} and magnetic field B. Purple regions indicate conductance plateaus, zero transconductance. Red/yellow/green/blue regions indicate increases in conductance when new subbands become available. White regions indicate negative transconductance. Colored boxes are guides to the eye indicating the location of highlighted conductance curves. **b**, Plot showing full conductance data. Conductance curves at 1 T intervals are highlighted in black and are offset for clarity. **c-e**, Conductance G as a function of side gate voltage V_{sg} curves at different out-of-plane magnetic field B values highlighting some fractional conductance features. T=15 mK.

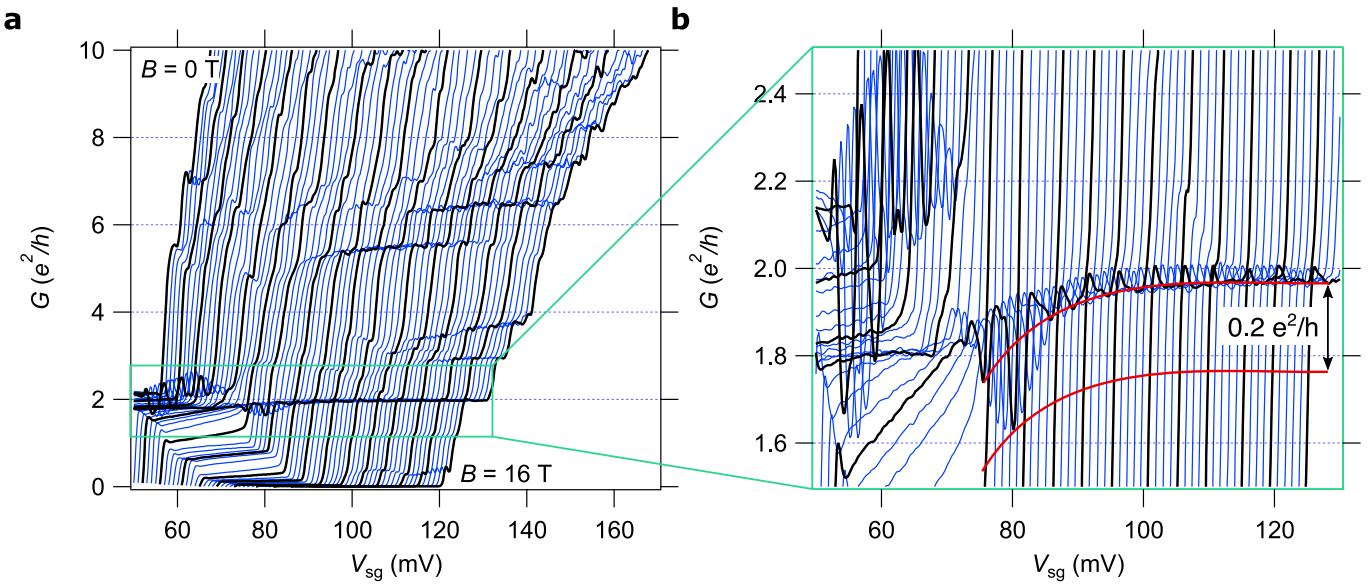

Extended Data Fig. 2 | Device B1 1.8 Feature. a, Conductance data - same as shown in Extended Data Fig. 1b. **b**, Zoom on region highlighting feature at $G \approx 1.8e^2/h$. Red lines are guides to the eye to show that the feature near 1.6 is in fact 0.2 below the $2e^2/h$ plateau, which itself is not fully resolved until the highest magnetic fields.

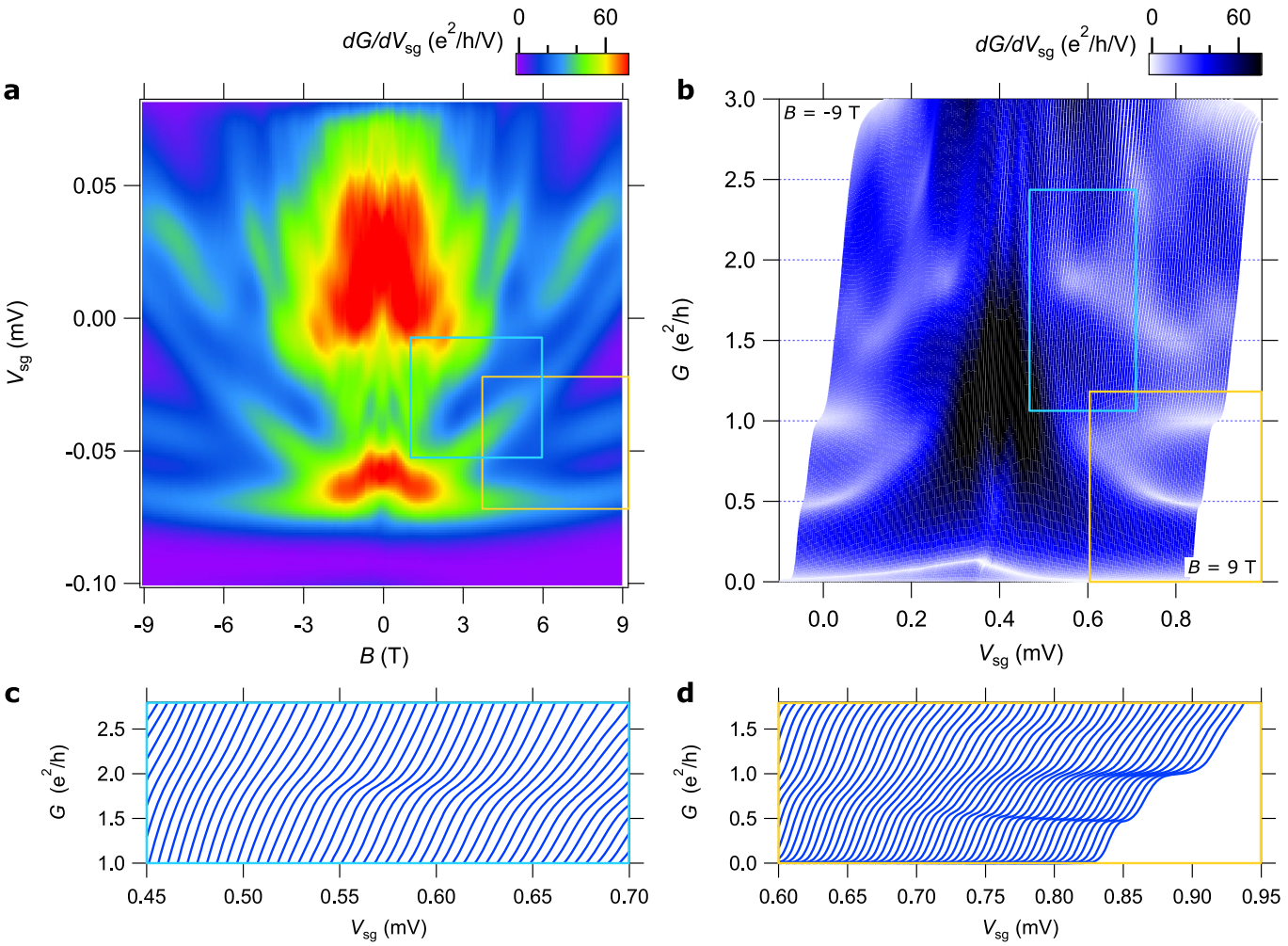

Extended Data Fig. 3 | Magnetotransport data for vertical superlattice Device B2. a, Transconductance map dG/dV_{sg} as a function of side gate voltage V_{sg} and magnetic field B. Purple regions indicate conductance plateaus, that is, zero transconductance. Red/yellow/green/blue regions indicate increases in conductance when new subbands become available. Colored boxes are guides to the eye indication the location of highlighted conductance curves. **b**, Plot showing full conductance data. Each curve is colored according to the transconductance at each side gate value (white indicates a plateau, black indicates rapidly increasing conductance). Curves are offset clarity. **c, d**, Conductance G as a function of side gate voltage V_{sg} curves at different out-of-plane magnetic field B values highlighting some fractional conductance features. T=50 mK.

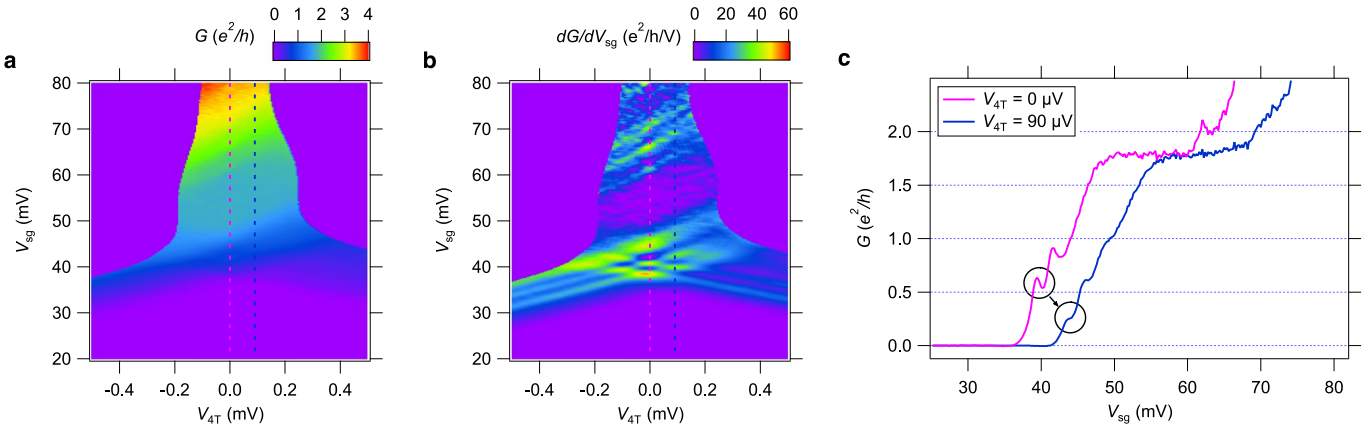

Extended Data Fig. 4 | Finite-bias spectroscopy. a, Conductance G intensity map as a function of four-terminal voltage V_{4t} and side gate voltage V_{sg}. Pink and blue dashed lines indicate the locations for the vertical linecuts shown in **c**. **b**, Transconductance (dG/dV_{sg}) intensity map as a function of four-terminal voltage V_{4t} and side gate voltage V_{sg}. The transconductance map shows the diamond features indicating ballistic transport in the superlattice devices. **c**, Vertical conductance linecuts at $V_{4t} = 0$ and $90 \approx \mu$V. Circles indicate fractional conductance values below the $(2e^2)/h$ plateau (corresponding to the lowest diamond features visible in the transconductance map in panel **b**) that become half of their value at a finite bias. Curves are offset for clarity. Data shown is from Device A and taken at $B = 13$ T and T=15 mK.

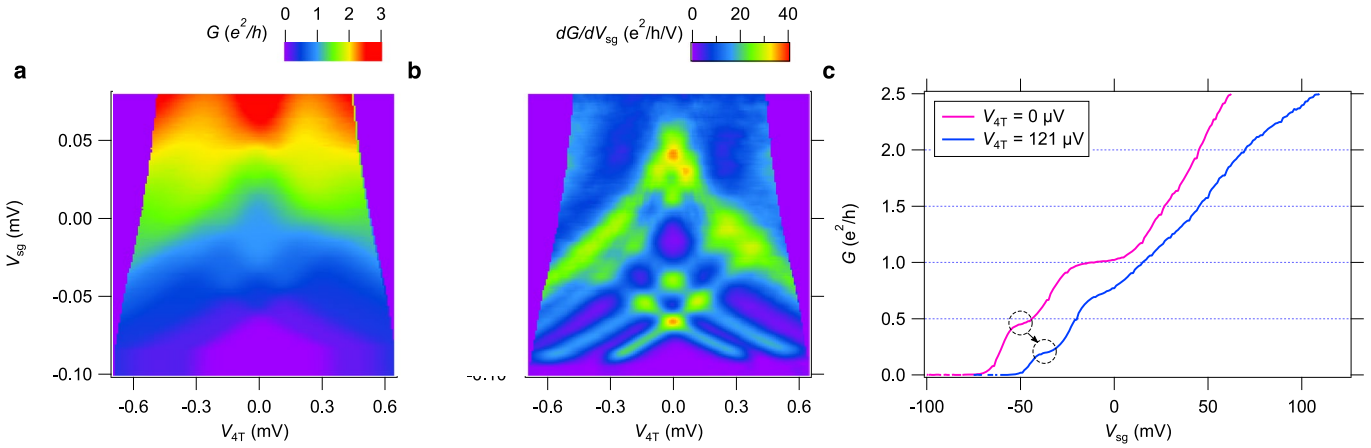

Extended Data Fig. 5 | Device B2 Finite Bias Spectroscopy. a, Conductance G intensity map as a function of four-terminal voltage V_{4t} and side gate voltage V_{sg}. Pink and blue dashed lines indicate the locations for the vertical linecuts shown in **c**. **b**, Transconductance (dG/dV_{sg}) intensity map as a function of four-terminal voltage V_{4t} and side gate voltage V_{sg}. The transconductance map shows the diamond features indicating ballistic transport in the superlattice devices. **c**, Vertical conductance linecuts at V_{4t}=0 and 121 μV. Circles indicate fractional conductance values below the $2e^2/h$ plateau (corresponding to the lowest diamond features visible in the transconductance map in panel **b**) that become half of their value at a finite bias. Curves are offset for clarity. Data shown is from Device B2 and taken at B = 9 T and T=50 mK.

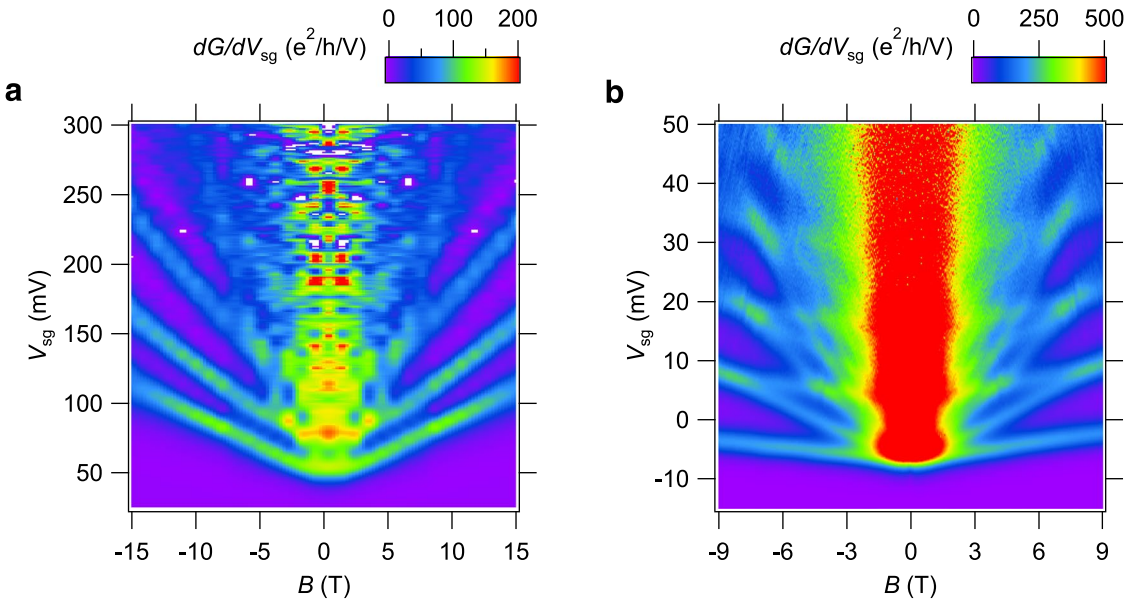

Extended Data Fig. 6 | Magnetotransport data for control electron waveguide devices. a, Transconductance map dG/dV_{sg} as a function of side gate voltage V_{sg} and magnetic field B for Device C1. Data previously published in ref. [3]. **b**, Transconductance map for Device C2. $T = 50$ mK.

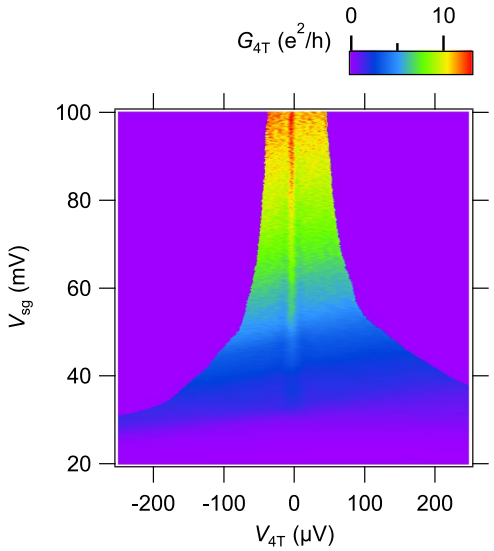

Extended Data Fig. 7 | Superconductivity in Device A. Conductance map G_{4t} as a function of side gate voltage V_{sg} and four-terminal voltage V_{4t}. A small increase of G_{4t} near $V_{4t} = 0\mu V$ is associated with superconductivity. B=0 T and T = 15 mK.